

# Predicting nonresonant pressure-driven MHD modes in equilibria with low magnetic shear

Cite as: Phys. Plasmas **28**, 012106 (2021); <https://doi.org/10.1063/5.0032489>

Submitted: 08 October 2020 • Accepted: 22 December 2020 • Published Online: 21 January 2021

 A. M. Wright,  N. M. Ferraro, S. R. Hudson, et al.

## COLLECTIONS

 This paper was selected as Featured



View Online



Export Citation



CrossMark

## ARTICLES YOU MAY BE INTERESTED IN

[A new explanation of the sawtooth phenomena in tokamaks](#)

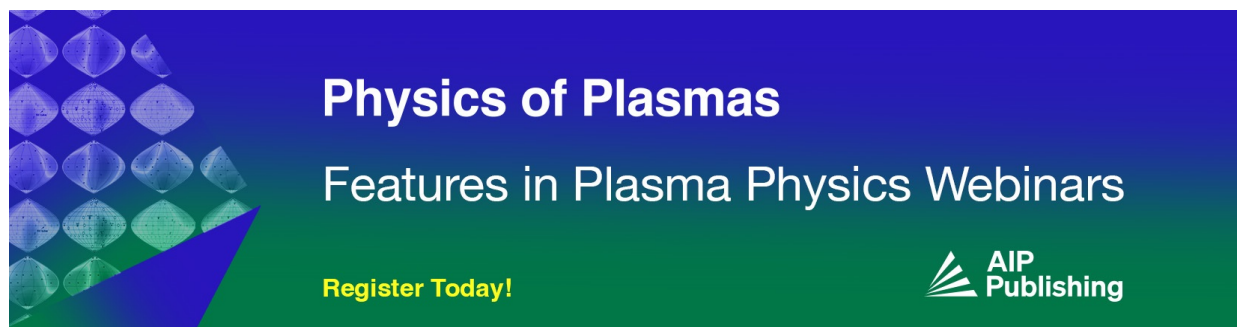
Phys. Plasmas **27**, 032509 (2020); <https://doi.org/10.1063/1.5140968>

[Mode spectrum characteristics and onset of the low-shear MHD stability regime](#)

Phys. Plasmas **28**, 072511 (2021); <https://doi.org/10.1063/5.0053870>

[Mechanisms of energetic-particle transport in magnetically confined plasmas](#)

Phys. Plasmas **27**, 030901 (2020); <https://doi.org/10.1063/1.5136237>



**Physics of Plasmas**  
Features in Plasma Physics Webinars

Register Today!



# Predicting nonresonant pressure-driven MHD modes in equilibria with low magnetic shear

Cite as: Phys. Plasmas **28**, 012106 (2021); doi: [10.1063/5.0032489](https://doi.org/10.1063/5.0032489)

Submitted: 8 October 2020 · Accepted: 22 December 2020 ·

Published Online: 21 January 2021



View Online



Export Citation



CrossMark

A. M. Wright,<sup>1,2,a)</sup>  N. M. Ferraro,<sup>1</sup>  S. R. Hudson,<sup>1</sup>  R. L. Dewar,<sup>2</sup>  and M. J. Hole<sup>2</sup> 

## AFFILIATIONS

<sup>1</sup>Princeton Plasma Physics Laboratory, PO Box 541, Princeton, New Jersey 08543, USA

<sup>2</sup>Mathematical Sciences Institute, Australian National University, Canberra, ACT 2601, Australia

<sup>a)</sup>Author to whom correspondence should be addressed: [awright@pppl.gov](mailto:awright@pppl.gov)

## ABSTRACT

Nonresonant internal modes can be difficult to anticipate as there is no resonant surface in the plasma. However, equilibria that are unstable to multiple nonresonant magnetohydrodynamic (MHD) modes may be more prone to global loss of confinement since these instabilities generate spatially extended linear displacements, potentially enhancing magnetic field line chaos via nonlinear interactions. Here, we successfully predict the unstable nonresonant pressure-driven modes for equilibria with zero shear in the plasma core, irrational  $q$  on axis, and a central pressure gradient, which is consistent with pre-crash profiles in sawtooth tokamak plasmas in the large-aspect-ratio limit. A criterion for identifying nonresonant modes most likely to be unstable is developed from the convergents of the continued fraction representation of  $q_0$ . A higher-order analysis of the standard Energy Principle reveals the conditions under which these modes are expected to dominate. Linear growth rate spectra, as a function of toroidal mode number (up to  $n = 30$ ), calculated using the initial-value extended-MHD code, M3D-C<sup>1</sup>, recover the characteristic dependence observed for ideal infernal modes. Nonresonant modes have also been invoked in some ideal sawtooth crash models. This work provides a mechanism to predict the mode numbers of infernal modes and, potentially, the width of some post-sawtooth-crash profiles.

Published under license by AIP Publishing. <https://doi.org/10.1063/5.0032489>

## I. INTRODUCTION

Linear stability analysis of internal modes in magnetohydrodynamics (MHD) typically focuses on resonant instabilities, that is, instabilities with poloidal and toroidal mode number,  $m$  and  $n$ , respectively, such that  $q = m/n$  somewhere in the plasma volume. One reason for this is because the effect of magnetic field line bending is—generally—strongly stabilizing everywhere except in the vicinity of a resonant surface, where it vanishes. Thus, a perturbation that decreases the potential energy and corresponds to a linear instability according to the standard Energy Principle<sup>1</sup> is most likely to be associated with resonant surfaces in the plasma.

In hybrid tokamak scenarios<sup>2</sup> and stellarators, where the magnetic shear can be small, the stabilizing effect of magnetic field line bending can also be small. Under these conditions, a perturbation may decrease the potential energy and lead to a linearly unstable  $(m, n)$  mode, even without a corresponding mode rational surface in the plasma.

Nonresonant modes are such that there is no resonant surface in the plasma so that  $q \neq m/n$ , for a given  $(m, n)$  mode under consideration. Nonresonant modes are associated with infernal modes in

tokamaks<sup>3–5</sup> as well as some models of the ‘crash’ phase of sawtooth cycles that invoke ideal instabilities.<sup>6–8</sup>

While resonant instabilities are generally localized about a resonant surface [a famous exception being the  $(m = 1, n = 1)$  mode], nonresonant instabilities are associated with spatially extended linear displacements resulting in global mode structures. Consequently, equilibria that are unstable to nonresonant modes may be more prone to global loss of confinement since spatial overlap of multiple linear radial mode structures can be associated with the generation of magnetic field line chaos due to nonlinear interactions.<sup>9</sup>

Due to their nonresonant nature, a key challenge is to predict which modes will be unstable. Doing so may also enable quantitative prediction of the spatial extent of chaotic field line regions generated via nonlinear interactions. This is important, for example, for determining the modes most likely to lead to loss of confinement and predicting the width of post-crash profiles in some sawtooth models.<sup>6</sup>

In this work, we investigate nonresonant pressure-driven MHD modes in the large-aspect-ratio limit of tokamak equilibria with zero shear and no resonances [i.e.,  $q_0 \equiv q(r = 0)$  is irrational] in the plasma core. In contrast to previous studies of nonresonant ideal

interchange modes,<sup>10,11</sup> we consider equilibrium pressure profiles that are peaked near the plasma core, consistent with previous infernal mode studies<sup>3</sup> and pre-crash profiles observed in sawtooth tokamak plasmas.<sup>12</sup> We calculate the growth rate spectrum  $\gamma(n)$ , where  $\gamma$  denotes the linear growth rate, for a range of  $q_0 > 1$ . In doing so, we demonstrate the existence of physically relevant parameter regimes where linear stability is dominated by fast-growing nonresonant modes with moderate to high  $n$  and infernal mode like  $\gamma(n)$  spectra.

This paper is subsequently organized as follows. In Secs. II and III, we describe the construction of the equilibrium profiles used in the present study, and how properties of the real numbers can be used to predict unstable nonresonant modes. In Sec. IV, we identify the conditions in which nonresonant instabilities are expected to dominate by performing a higher-order analysis of the Energy Principle using the nonresonance parameter,  $\delta q \equiv |q - m/n|$ , as an expansion parameter. In Sec. V, we present results of linear parameter scans performed using the initial-value extended-MHD code, M3D-C<sup>13</sup> that validate the predictions and compute  $\gamma(n)$  spectra. Discussions and conclusions are presented in Sec. VI.

## II. EQUILIBRIUM PROFILES

As the primary focus of this work is on tokamak equilibria in the large-aspect-ratio limit, we consider a periodic cylinder of length,  $L = 2\pi R_0$ , where  $R_0$  is the major radius,  $a$  is the minor radius, and  $\varepsilon \equiv a/R_0 \ll 1$  is the inverse aspect ratio. To construct equilibria with zero shear and no resonances in the plasma core, we use the method developed by Hudson and Kraus<sup>14</sup> and Wright *et al.*<sup>15</sup> In this fixed boundary model, external modes are precluded by construction, and we require  $\mathbf{B} \cdot \hat{\mathbf{n}} = 0$  at  $r = a$ , where  $\mathbf{B}$  is the magnetic field.

As in Wright *et al.*,<sup>15</sup> we refer to regions where  $\nabla p \neq 0$  and  $\nabla p = 0$  as the “ideal” and “relaxed” regions, respectively, noting that this serves simply as a concise label for the presence or otherwise of gradients in the pressure profile and should not be confused with stability properties of the equilibria. We introduce a normalized radial coordinate,  $x = r/a$ , such that  $0 \leq x \leq 1$  and partition the domain,  $\mathcal{R} = \{x : x \in [0, 1]\}$ , into three sub-domains such that  $\mathcal{R} = \mathcal{R}_1 \cup \mathcal{R}_2 \cup \mathcal{R}_3$ , where

$$\mathcal{R}_1 = \{x : x \in [0, x_1]\}, \tag{1}$$

$$\mathcal{R}_2 = \{x : x \in [x_1, x_2]\}, \tag{2}$$

$$\mathcal{R}_3 = \{x : x \in [x_2, 1]\}, \tag{3}$$

for some constants  $x_1$  and  $x_2$  such that  $0 < x_1 < x_2 < 1$ . For this work, we choose  $\mathcal{R}_1$  and  $\mathcal{R}_3$  to be ideal regions and  $\mathcal{R}_2$  to be relaxed. In the ideal regions, the pressure profile is given by a cubic polynomial in  $x$  with  $p(x = 0) \equiv p_0$  and  $p(x = 1) \equiv p_2$ , with the remaining degrees of freedom chosen such that the internal matching conditions, described later, are satisfied. In the relaxed region,  $\mathcal{R}_2$ , the pressure is a prescribed constant,  $p_1$ . Negative pressure gradients are well known to be destabilizing so to ensure Suydam’s criterion is satisfied at every resonant surface, we choose the  $q$ -profile in the ideal regions (where  $\nabla p \neq 0$ ) to be a constant and *irrational*. Specifically, we prescribe  $q(x = 0) \equiv q_0$  and  $q(x = 1) \equiv q_{edge}$  to be the value of  $q$  in  $\mathcal{R}_1$  and  $\mathcal{R}_3$ , respectively.

In the ideal regions (where  $\nabla p \neq 0$ ), the 1D equilibrium satisfies

$$\frac{d}{dx} \left[ \mu_0 p(x) + \frac{1}{2} \left( \frac{\varepsilon^2 x^2}{q^2} + 1 \right) B_z^2(x) \right] + \frac{\varepsilon^2 x}{q^2} B_z^2(x) = 0, \tag{4}$$

where  $q = \varepsilon x B_z / B_\theta$ . In the relaxed regions (where  $\nabla p = 0$ ), the equilibrium satisfies

$$\frac{dB_z(x)}{dx} = -\alpha B_\theta(x), \tag{5}$$

$$\frac{B_\theta(x)}{x} + \frac{dB_\theta(x)}{dx} = \alpha B_z(x), \tag{6}$$

which admits the general solutions

$$B_\theta = cJ_1(\alpha x) + dY_1(\alpha x), \tag{7}$$

$$B_z = cJ_0(\alpha x) + dY_0(\alpha x), \tag{8}$$

where  $J_l(x)$  and  $Y_l(x)$  are Bessel functions of the first and second kind, respectively, while  $c$ ,  $d$ , and  $\alpha$  are constants.

We solve Eqs. (4)–(6) independently in the respective regions. To complete the construction of the global equilibrium profiles, we require  $p$ ,  $\nabla p$ ,  $B_z$ , and  $q$  to be continuous at the internal boundaries,  $x_1$  and  $x_2$ . The first two conditions complete the specification of the pressure profile and ensure  $p \in C^1$ , i.e., its first derivative exists and is continuous. The internal matching conditions ensure continuity of the total pressure,  $p + B^2/2\mu_0$ , which means that there are no current sheets in the equilibria, despite discontinuities in  $J_z$ .

Typical equilibrium profiles used for the present study are given in Fig. 1, with corresponding parameter values summarized in Table I. To investigate the role of nonresonance and pressure gradient localization in the plasma core, we vary  $q_0$  and  $x_1$  while keeping remaining parameters fixed. By choosing to partition the domain,  $\mathcal{R}$ , into three sub-domains rather than two, we are able to accommodate more realistic edge pressure profiles while simultaneously avoiding resonant pressure-driven modes near the plasma edge. The effect of  $q$ -profile flattening near the plasma edge on stability has been examined in detail previously<sup>16</sup> but is largely unimportant for the present work.

## III. PREDICTING NONRESONANT MODES FROM PROPERTIES OF THE REAL NUMBERS

We now describe the approach employed in this study for choosing the values of  $q_0$ . Together with the fact that some irrationals are better approximated by rationals than others, we discuss how this can be used to predict the nonresonant modes most likely to be unstable.

Since we are interested in the effect of strictly nonresonant modes, we choose  $q_0$  to be irrational, meaning there are no pairs of integers,  $m$  and  $n$ , such that  $q_0 = m/n$  in the zero-shear region. However, from the density of the rationals,  $\mathbb{Q}$ , in  $\mathbb{R}$ , it follows that between any pair of distinct irrational numbers, there exist infinitely many rationals.<sup>17</sup> Thus, although  $q_0$  is strictly irrational, it may be well approximated by a nearby rational. Physically, this means that if  $m/n$  is a good approximation of  $q_0$ , the corresponding  $(m, n)$  mode may be unstable even though  $q_0 \neq m/n$ . We now describe one way to construct rational approximations of irrationals and how to quantify the notion of a good approximation.

Every real number,  $\zeta$ , can be represented as a continued fraction, i.e.,

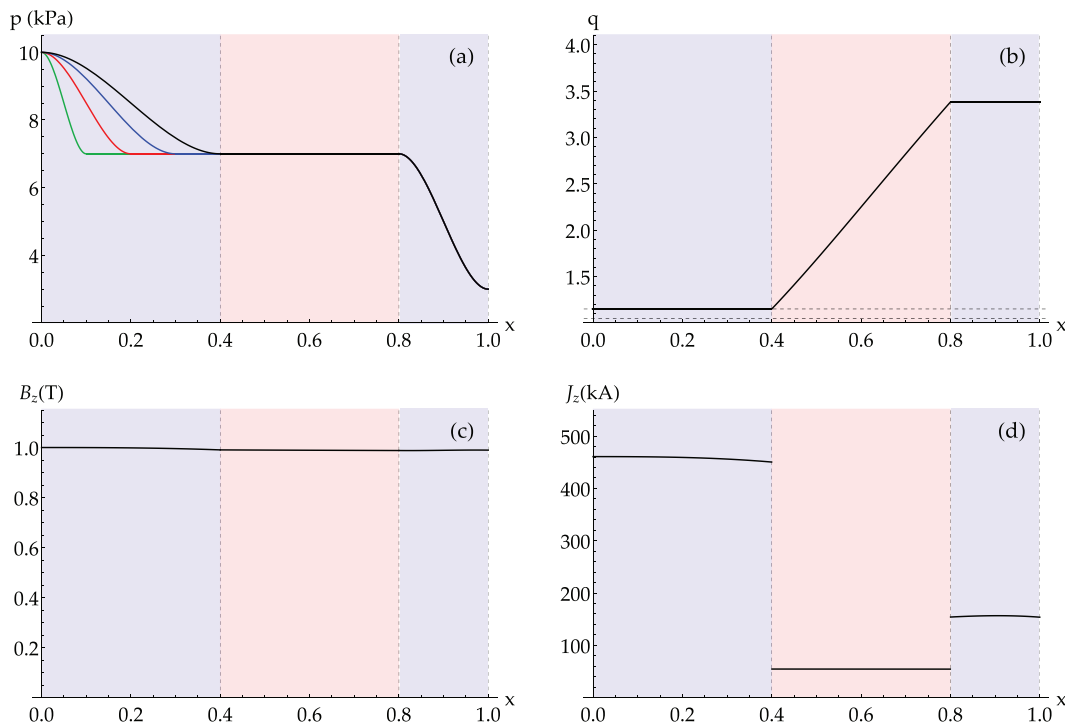


**FIG. 1.** Equilibrium profiles with tokamak-like parameter values given in Table I; (a) pressure profile, (b)  $q$ -profile, (c) axial magnetic field, and (d) axial current density. The internal boundaries ( $x = x_1, x_2$ ) and plasma edge ( $x = 1$ ) are denoted by vertical dashed lines. The ideal and relaxed regions are shaded blue and red, respectively. To vary localization of the pressure gradient in the core region, we fix  $p_0$  and vary  $x_1$ , the effect of which is illustrated in (a) with  $x_1 = 0.4$  (black), 0.3 (blue), 0.2 (red), and 0.1 (green). In (b), the minimum and maximum values of  $q_0$  considered are denoted by horizontal dashed lines.

$$\chi = a_0 + \frac{b_1}{a_1 + \frac{b_2}{a_2 + \frac{b_3}{a_3 + \dots}}}$$

where  $a_{i-1}$  and  $b_i$  are some integers for  $i \geq 1$ . If a continued fraction terminates after some finite  $i$ , then  $\chi$  is a rational. Otherwise,  $\chi$  is irrational. Truncating the continued fraction representation of an irrational number at some finite  $i$  yields a rational number known as a

**TABLE I.** A summary of the equilibrium parameter values used throughout the present work. Here,  $\varphi = (1 + \sqrt{5})/2 \approx 1.618$  is the golden ratio.

Parameter	Value
$x_1$	[0.1, 0.4]
$x_2$	0.8
$p_0$	$1 \times 10^4$ Pa
$p_1$	$0.7 \times 10^4$ Pa
$p_2$	$0.3 \times 10^4$ Pa
$q_0$	Variable
$q_{edge}$	$\frac{4 + 3\varphi}{1 + \varphi} \approx 3.38197$
$a/R_0$	1/3
$B_0$	1 T

convergent,  $c_i$ . The sequence of convergents,  $(c_i)_{i \geq 1}$ , is one systematic approach to constructing rational approximations of irrational numbers. In this work, we investigate modes associated with convergents of each  $q_0$  that satisfy a particularly stringent property, which we now describe.

Consider some  $\chi \in \mathbb{R} \setminus \mathbb{Q}$  and all  $m, n \in \mathbb{Z}$ . Denote by  $E_{m,n}$  the absolute error associated with approximating  $\chi$  by the rational  $m/n$ , i.e.,

$$E_{m,n} \equiv \left| \chi - \frac{m}{n} \right|. \tag{9}$$

We call  $m$  and  $n$  co-prime if the greatest common divisor of  $m$  and  $n$  is 1. By Hurwitz's theorem,<sup>18</sup> we know that for every irrational number,  $\chi$ , there are infinitely many co-prime integers,  $m$  and  $n$ , such that

$$E_{m,n} \equiv \left| \chi - \frac{m}{n} \right| < M_n \equiv \frac{1}{\sqrt{5}n^2}. \tag{10}$$

Figure 2 illustrates the distribution of all co-prime pairs  $(m,n)$  for  $m, n \leq 30$ . In this work, we consider  $m/n$  to approximate  $\chi$  arbitrary well (and therefore most likely to be unstable) if  $E_{m,n}/M_n \approx 0$  and conversely,  $m/n$  is a poor approximation of  $\chi$  (least likely to be unstable) if  $E_{m,n}/M_n \approx 1$ .

Every  $m/n$  satisfying Eq. (10) is a convergent of  $\chi$  but not every convergent of  $\chi$  satisfies Eq. (10).<sup>18</sup> Hurwitz's theorem, Eq. (10), gives the most stringent upper bound on  $E_{m,n}$  such that there are still

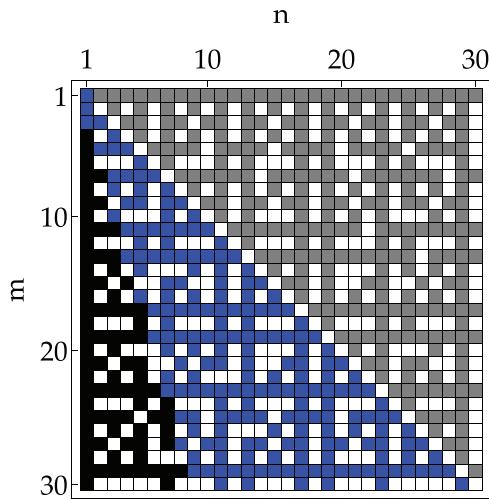


FIG. 2. Shaded cells denote co-prime pairs  $(m,n)$  for  $m,n \leq 30$  with  $m/n < 1$  (gray),  $1 \leq m/n < q_{edge}$  (blue), and  $m/n > q_{edge}$  (black).

infinitely many admissible co-prime pairs,  $(m,n)$ . Using this fact as a criterion for identifying potentially unstable nonresonant modes, henceforth, we consider modes associated with convergents of each  $q_0$  satisfying Eq. (10).

As part of the numerical studies presented in Sec. V, we consider properties of modes associated with specific convergents over a range of  $q_0$ . Hence, for each  $q_0$ , the modes under consideration have different poloidal and toroidal mode numbers. We use condition Eq. (10)—an elementary and well-known result—as a tool to guide which convergents and/or modes to consider within the scope of the present work. That is, of course, not to say that *only* modes associated with convergents satisfying Eq. (10) are unstable. For the reader’s benefit, we preempt the findings of Sec. V and remark while modes associated with convergents satisfying Eq. (10) are, indeed, unstable, so too are those of convergents which are poorer approximations of  $q_0$  in the sense of Eq. (10). This motivates the development of additional criteria which exploit properties of continued fractions, as is being pursued in ongoing work.

For this work, we are interested in  $q_0$  close to but above unity since this corresponds to the conditions considered in previous studies of infernal modes<sup>3,4</sup> and ideal sawtooth crash models.<sup>6,8</sup> We choose irrational  $q_0$  parameterized by an integer  $b$  and given by

$$q_0(b) = \frac{1 + b\varphi}{1 + (b - 1)\varphi} = 1 + \frac{1}{b + \frac{1}{2}(\sqrt{5} - 3)}, \quad (11)$$

where  $\varphi = (1 + \sqrt{5})/2 \approx 1.618$  is the golden ratio and well known to be the “most” irrational number.<sup>18</sup> For each  $b$ , the irrational  $q_0(b)$  admits a continued fraction representation from which the convergents can be determined. Throughout this work, we consider  $b \in [7, 20] \subset \mathbb{Z}$  which corresponds to  $1.051 \lesssim q_0 \lesssim 1.1511$ . For comparison, the nonlinear simulations by Kirby<sup>8</sup> of zero central shear  $q$ -profiles considered  $q_0 = 1.04$  and  $q_0 = 1.005$ .

For each  $q_0(b)$  with  $b \geq 7$ , the sequence of convergents,  $(q_{0,i})_{i \geq 1}$ , satisfying Eq. (10) is given by

$$(q_{0,1}, q_{0,2}, q_{0,3}, q_{0,4}, \dots) = \left( \frac{1}{1}, \frac{b+1}{b}, \frac{3b+2}{3b-1}, \frac{8b+5}{8b-3}, \dots \right). \quad (12)$$

For example,

$$b = 7 : (q_{0,1}, q_{0,2}, q_{0,3}, q_{0,4}, \dots) = \left( \frac{1}{1}, \frac{8}{7}, \frac{23}{20}, \frac{61}{53}, \dots \right), \quad (13)$$

$$b = 8 : (q_{0,1}, q_{0,2}, q_{0,3}, q_{0,4}, \dots) = \left( \frac{1}{1}, \frac{9}{8}, \frac{26}{23}, \frac{69}{61}, \dots \right), \quad (14)$$

$$b = 9 : (q_{0,1}, q_{0,2}, q_{0,3}, q_{0,4}, \dots) = \left( \frac{1}{1}, \frac{10}{9}, \frac{29}{26}, \frac{77}{69}, \dots \right), \quad (15)$$

$$b = 10 : (q_{0,1}, q_{0,2}, q_{0,3}, q_{0,4}, \dots) = \left( \frac{1}{1}, \frac{11}{10}, \frac{32}{29}, \frac{85}{77}, \dots \right). \quad (16)$$

Each  $q_{0,i}$  is, thus, associated with a nonresonant  $(m,n)$  mode, which we predict is likely to be unstable. Specifically, the numerator and denominator of each  $q_{0,i}$  correspond, respectively, to the poloidal and toroidal mode number of the associated instability.

In Fig. 3, we compare  $E_{m,n}/M_n$  for  $1.051 \lesssim q_0 \lesssim 1.1511$  corresponding to  $b \in [7, 20]$  for the first three elements of the sequence defined by Eq. (12). In Fig. 4, we compare  $E_{m,n}/M_n$  for the first seven elements of  $(q_{0,i})_{i \geq 1}$  for  $b = 7, 8, 9$ , and 10. We find that for  $i \geq 3$ ,  $E_{m,n}/M_n \approx 1$  indicating that there are a few relatively low order rationals which can reasonably approximate  $q_0$ , as expected. Moreover, we find that  $q_{0,1}$  is, relatively speaking, the best approximation since  $E_{m,n}/M_n$  is smallest. The upper bound on the error of the rational approximation,  $M_n$ , goes like  $n^{-2}$ . To maintain  $E_{m,n}/M_n$  close to zero as  $n$  increases requires  $E_{m,n}$  to become very small.

#### IV. HIGHER-ORDER ANALYSIS OF THE STANDARD ENERGY PRINCIPLE FOR NONRESONANT MODES

Since the  $(m = 1, n = 1)$  mode leads to a gross displacement of the magnetic axis and  $|q - 1| \ll 1$ , one might intuitively expect it to be the most important ‘nearby’ mode, even if there is no  $q = 1$  surface in the plasma. Thus, previous analyses of the quasi-interchange instability focused on the nonresonant  $(1,1)$  mode in low shear equilibria.<sup>7,8,19–21</sup>

On the other hand, infernal modes tend to have higher poloidal and toroidal mode numbers.<sup>3</sup> These modes are so named because even though the Mercier criterion is satisfied and standard ballooning

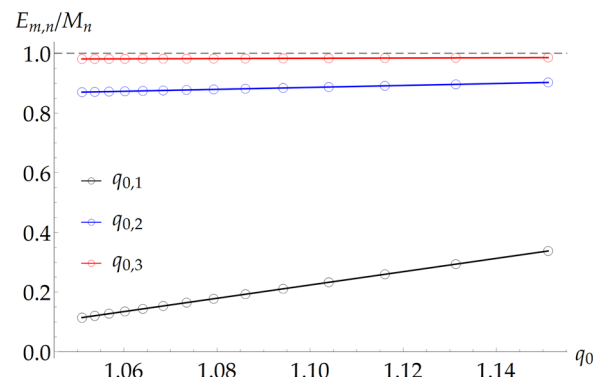
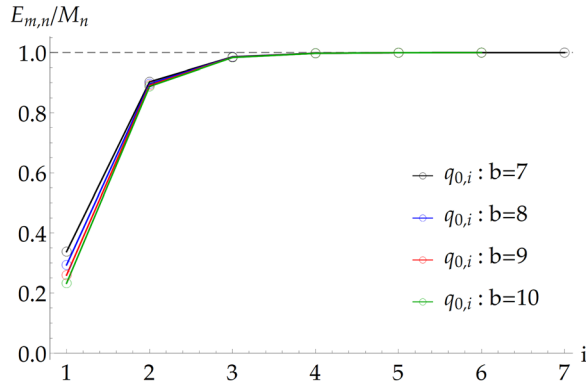


FIG. 3. Relative error defined according to Eq. (10), with  $b \in [7, 20]$  for  $q_{0,1} = 1/1$  (black) and  $q_{0,2} = (b + 1)/b$  (blue), and  $q_{0,3} = (3b + 2)/(3b - 1)$  (red).



**FIG. 4.** Relative error defined according to Eq. (10) for the first seven elements of the sequence defined by Eq. (12) for  $b = 7$  (black),  $b = 8$  (blue),  $b = 9$  (red), and  $b = 10$  (green).

theory predicts stability, when shear is low the plasma turns out to be unstable nonetheless. Since interchange and ballooning theory are used to constrain the maximum plasma  $\beta$ , the existence of infernal modes may necessitate more pessimistic stability boundaries.<sup>3,4</sup>

To provide a unified understanding of nonresonant pressure-driven modes and determine when they are likely to be important, we perform a higher-order analysis of the standard Energy Principle for internal modes.<sup>1</sup> We explicitly treat the nonresonance parameter,  $\delta q \equiv |q - m/n|$ , which allows us to tease out connections between nonresonance, quasi-interchange modes and selected characteristics of infernal modes. In doing so, we derive thresholds for the critical central pressure gradient, which are validated by subsequent M3D-C<sup>1</sup> calculations. Note that if we replace  $q$  with the irrational,  $\chi$ , then  $\delta q$  is exactly  $E_{m,n}$  as given by Eq. (9).

In the large-aspect-ratio tokamak limit, the standard Energy Principle is given by<sup>22</sup>

$$\delta W = \frac{2\pi^2 R_0}{\mu_0} \int_0^1 \left[ \frac{x\tilde{F}^2}{\tilde{k}_0^2} \left( \frac{d\zeta(x)}{dx} \right)^2 + \frac{\tilde{g}(x)}{\tilde{k}_0^2} \zeta^2(x) \right] dx, \quad (17)$$

where

$$\tilde{g} = 2\mu_0 \lambda^2 \frac{dp}{dx} + \frac{\tilde{k}_0^2 x^2 - 1}{x} \tilde{F}^2 + \frac{2\lambda^2 \tilde{F} \tilde{F}^\dagger}{x \tilde{k}_0^2}, \quad (18)$$

$$\tilde{F} = \lambda B_z + \frac{m B_\theta}{x}, \quad (19)$$

$$\tilde{F}^\dagger = \lambda B_z - \frac{m B_\theta}{x}, \quad (20)$$

$$\tilde{k}_0^2 = \lambda^2 + \frac{m^2}{x^2}, \quad (21)$$

with  $\lambda \equiv ka = -\epsilon n$  and  $\zeta(x) = \xi \cdot \hat{r}$  is the radial displacement.

We consider an expansion in  $\lambda$  such that

$$\delta W = \delta W_0 + \lambda^2 \delta W_2 + \lambda^4 \delta W_4 + \dots, \quad (22)$$

and proceed to investigate the behavior of  $\delta W$  order by order. Note that typically,<sup>22,23</sup>  $\delta W$  is expanded in orders of  $\epsilon^2$ . For  $n \sim \mathcal{O}(1)$ ,

$\mathcal{O}(\lambda) \sim \mathcal{O}(\epsilon)$  and, thus,  $\lambda \ll 1$  is a suitable expansion parameter. As  $n$  increases, however,  $\epsilon$  must decrease further in order to maintain  $\lambda \ll 1$ .

The  $\mathcal{O}(\lambda^2)$  term of  $\delta W$  can be written as

$$\delta W_2 = W_0 \int_0^1 \frac{x B_z^2 \delta q^2}{m^2 q^2} \left[ x^2 \left( \frac{d\zeta}{dx} \right)^2 + (m^2 - 1) \zeta^2 \right] dx, \quad (23)$$

where

$$W_0 = \frac{2\pi^2 R_0}{\mu_0}. \quad (24)$$

For  $i \geq 2$ , we have

$$\begin{aligned} \lambda^{2i} \delta W_{2i} = & (-1)^i \lambda^{2i} W_0 \int_0^1 \frac{x^{2i-1} B_z^2}{m^{2i} q^2} \left[ -x^2 \delta q^2 \left( \frac{d\zeta}{dx} \right)^2 \right. \\ & \left. + \left( \left( \frac{m}{n} \right)^2 \frac{2\mu_0 x dp}{B_\theta^2 dx} + \delta q \left( (2i-1)q + \frac{(2i-3)m}{n} \right) \right) \zeta^2 \right] dx. \end{aligned} \quad (25)$$

Note that the “straight tokamak” model employed in this study is generally valid for low- $\beta$  equilibria.<sup>22</sup> In the expansion considered presently, this is implicitly manifest by the fact that the pressure gradient does not appear until at least  $\mathcal{O}(\lambda^4)$ . Importantly, the contribution of the pressure drive at each order is independent of  $\delta q$ . We now discuss how two effects, which impact pressure-driven modes, are related to nonresonance.

### A. Impact of nonresonance on pressure-driven instabilities

In this system, the overall drive comes from the pressure gradient which is such that  $\nabla p < 0$ , and thus destabilizing in  $\mathcal{R}_1$ . Since we fix  $p_0$  and  $p_1$ , the value of  $p$  on the axis and at  $x = x_1$ , respectively, the maximum value of  $p'$  in  $\mathcal{R}_1$  must increase as  $x_1$  decreases. Here,  $'$  denotes differentiation with respect to  $x$ . In  $\mathcal{R}_1$ , it follows that

$$p' = \frac{6\Delta p}{x_1^3} x(x - x_1), \quad (26)$$

$$p'' = \frac{6\Delta p}{x_1^3} (2x - x_1), \quad (27)$$

where  $\Delta p = p_0 - p_1$ . Hence,  $p'$  is maximized at  $x = x_1/2$  and

$$\max p' = -\frac{3\Delta p}{2x_1}. \quad (28)$$

We now discuss some impacts of nonresonance on pressure-driven modes in the context of established results for such instabilities. Suydam’s criterion,<sup>24</sup> which determines stability with respect to (pressure driven) interchange modes in cylindrical geometry, is exact inasmuch that it is constructed from Eq. (17) by retaining terms of all orders. The criterion, however, is evaluated exactly at a resonant surface,  $x_s$ , which is such that  $q(x_s) = m'/n'$  for some integers  $m'$  and  $n'$ . For a given resonant surface,  $x_s$ , the Suydam approximation, from which Suydam’s criterion is derived, applies in the neighborhood  $|x - x_s| \sim 1/m'$  in the limit  $m', n' \rightarrow \infty$ .<sup>10</sup> A detailed discussion of

the eigenvalue spectrum for interchange instabilities was given by Dewar *et al.*<sup>10</sup> As noted by Shafranov,<sup>23</sup> about each resonance,  $n'q = m'$ , there is a band of values which may also be unstable for  $m' \neq 1$ . This follows from noting that the coefficient  $\tilde{g}$  of Eq. (17) is quadratic in  $n'q$  and can be solved to find the roots which, in turn, determines the region about which the equation has  $\tilde{g} < 0$ . In the standard case where  $q'$  is not small, the stabilizing effect of  $\tilde{F}$  dominates. Consequently, even when  $q'$  is small but nonzero, Eq. (17) is still positive throughout most of the plasma due to the stabilizing effect of shear. Instability can generally only arise when  $\tilde{F}$  is small, which is typically localized to a small region about the resonant surface where  $\tilde{F} = 0$ .

For a given resonance,  $q(x_s) = m'/n'$ , it is more likely for higher-order rationals to be nearby enough to  $m'/n'$  such that the corresponding mode is driven unstable by a non-local effect of the pressure gradient. These correspond to instabilities with higher poloidal and toroidal mode numbers. Simultaneously, however, high- $n$  interchange modes are typically well stabilized by magnetic field shear. For reduced shear scenarios, like those considered presently, we expect these nonresonant high- $n$  modes to be highly susceptible to being destabilized by a non-local pressure drive.

Another effect was described by Waelbroeck and Hazeltine<sup>19</sup> and manifests due to a breakdown of the ordering assumed in Eq. (22) when shear is small. In the standard case, from Eq. (23), it is clear that  $\delta W_2 > 0$  and, thus, the equilibrium are ideally stable (to internal modes) if  $q > 1$ , which can be guaranteed for a monotonic increasing  $q$  profile if  $q(0) > 1$ . For  $m = 1$ , a trial function can be constructed such that  $\delta W_2 \rightarrow 0$  and, thus, stability must be determined by an examination of the  $\mathcal{O}(\lambda^4)$  term. Since both the current and pressure gradient are destabilizing,  $\delta W_4 < 0$  and the equilibrium are unstable.

In the standard case,  $\delta q \sim \mathcal{O}(1)$  meaning  $\delta q \gg \varepsilon$  and, therefore,  $\delta q \gg \lambda$  when  $n \sim \mathcal{O}(1)$  or  $\varepsilon \rightarrow 0$  for large  $n$  away from the resonant surface, where  $\delta q$  vanishes. Interchange instabilities are, therefore, highly localized about the resonant surface since the pressure drive becomes dominant only when higher-order contributions to Eq. (22) are necessary.

In low shear scenarios, the breakdown in the ordering of Eq. (22) becomes global since  $\delta q \ll 1$  over an extended region of the plasma volume. Correspondingly, pressure-driven interchange instabilities cease to be local and, instead, generate global displacements. In the nonlinear regime, interactions between displacements associated with multiple non-localized modes may tend to lead to the generation of magnetic field line chaos across a significant region of the plasma, making these modes more dangerous from the point of view of plasma performance. Infernal modes have also been associated with a breakdown of the standard Energy Principle parameter ordering<sup>19,25</sup> and understood as a breakdown of standard ballooning theory<sup>3</sup> due to a low central shear  $q$ -profile.

### B. Predicting the critical pressure gradient for the ( $m = 1, n = 1$ ) nonresonant mode

We now consider Eq. (17) for strictly nonresonant modes so that  $\delta q \neq 0$  throughout the plasma volume of interest. We examine how varying  $\delta q$  for arbitrary  $m$  and  $n$  affects the ordering of Eq. (22), enables the identification of unstable modes, and constrains the maximum pressure gradient which can be sustained. In examining the balance of terms comprising Eq. (17), from which we, in turn, infer stability or otherwise of the plasma, for the ( $m = 1, n = 1$ ) mode we implicitly

assume  $\xi$  resembles the quasi-interchange mode eigenfunction,<sup>19</sup> which is relatively flat in the central plasma region and smoothly decreases to zero.

Substituting Eqs. (23) and (25) into Eq. (22), we can write

$$\begin{aligned} \frac{\delta W}{W_0} = & \sum_{i=1}^{\infty} \left[ (-1)^{i+1} \lambda^{2i} \int_0^1 \left( \frac{x^{2i+1} B_z^2}{m^{2i} q^2} \right) \delta q^2 \left( \frac{d\xi}{dx} \right)^2 dx \right. \\ & + \sum_{i=2}^{\infty} \left[ (-1)^i \lambda^{2i} \int_0^1 \left( \frac{x^{2i-1} B_z^2}{m^{2i} q^2} \right) \delta q \left( (2i-1)q + \frac{(2i-3)m}{n} \right) \xi^2 dx \right. \\ & + \lambda^2 \int_0^1 \frac{x B_z^2 \delta q^2}{m^2 q^2} (m^2 - 1) \xi^2 dx \\ & \left. + \sum_{i=1}^{\infty} \left[ (-1)^{i+1} \lambda^{2i} \int_0^1 \left( \frac{x}{m} \right)^{2i} \left( 2\mu_0 \frac{dp}{dx} \right) \xi^2 dx \right] \right]. \end{aligned} \quad (29)$$

From Eq. (29), the well-known limits are readily recovered. When  $\delta q \sim \mathcal{O}(1)$ , the perturbation expansion given by Eq. (22) is uniformly valid if  $2\mu_0 p' \sim \mathcal{O}(\lambda)$  or smaller, so that the  $i = 1$  contribution in the final term of Eq. (29) is at least  $\mathcal{O}(\lambda^3)$ . For  $B_z \approx \text{constant}$  and  $B_z \sim \mathcal{O}(1)$ , this corresponds to requiring  $\beta'_t \sim \mathcal{O}(\lambda)$ , where  $\beta_t = 2\mu_0 p/B_z^2$  is like the toroidal plasma  $\beta$ . When  $\delta q = 0$ , Eq. (29) reduces to

$$\frac{\delta W}{W_0} = \sum_{i=1}^{\infty} \left[ (-1)^{i+1} \lambda^{2i} \int_0^1 \left( \frac{x}{m} \right)^{2i} \left( 2\mu_0 \frac{dp}{dx} \right) \xi^2 dx \right], \quad (30)$$

which is just Eq. (17) with  $\tilde{F} = 0$ .

Setting  $\bar{\varepsilon} = \lambda/m$ , and we can write Eq. (29) as

$$\begin{aligned} \frac{\delta W}{W_0} = & \sum_{i=1}^{\infty} \left[ (-1)^{i+1} \bar{\varepsilon}^{2i} \int_0^1 \left( \frac{x^{2i+1} B_z^2}{q^2} \right) \delta q^2 \left( \frac{d\xi}{dx} \right)^2 dx \right. \\ & + \sum_{i=2}^{\infty} \left[ (-1)^i \bar{\varepsilon}^{2i} \int_0^1 \left( \frac{x^{2i-1} B_z^2}{q^2} \right) \delta q \left( (2i-1)q + \frac{(2i-3)m}{n} \right) \xi^2 dx \right. \\ & + \bar{\varepsilon}^2 \int_0^1 \frac{x B_z^2 \delta q^2}{q^2} (m^2 - 1) \xi^2 dx \\ & \left. + \sum_{i=1}^{\infty} \left[ (-1)^{i+1} \bar{\varepsilon}^{2i} \int_0^1 x^{2i} \left( 2\mu_0 \frac{dp}{dx} \right) \xi^2 dx \right] \right]. \end{aligned} \quad (31)$$

Using Eq. (26), the final term of Eq. (31) becomes

$$\begin{aligned} & \sum_{i=1}^{\infty} \left[ (-1)^{i+1} \bar{\varepsilon}^{2i} \int_0^1 \left( \frac{12\mu_0 \Delta p}{x_1^3} \right) x^{2i+1} (x - x_1) \xi^2 dx \right] \\ & \approx \sum_{i=1}^{\infty} \left[ (-1)^{i+1} \left( \frac{0.045 \bar{\varepsilon}^{2i}}{x_1^3} \right) \int_0^1 x^{2i+1} (x - x_1) \xi^2 dx \right], \end{aligned} \quad (32)$$

with values from Table I.

In Fig. 5, we plot the error,  $E_{m,n}$  defined by Eq. (10) for  $q_{0,1} - q_{0,4}$ . For the values of  $q_0$  considered,  $q_{0,1}$  and  $q_{0,2}$  mostly satisfy  $\mathcal{O}(\bar{\varepsilon}^6) \leq \delta q < \mathcal{O}(\bar{\varepsilon})$ . From Figs. 3 and 4, it is clear that apart from  $q_{0,1} = 1/1$  where  $E_{1,1} \approx \varepsilon M_1$ , we have  $E_{m,n}(q_{0,i}) \approx M_n = 1/(\sqrt{5n^2})$  for  $i > 1$ .

For  $q_{0,1}$  which corresponds to ( $m = 1, n = 1$ ), we have  $E_{1,1} \approx 0.15$  which implies  $\mathcal{O}(\bar{\varepsilon}^2) < \delta q < \mathcal{O}(\bar{\varepsilon})$ , which is somewhat

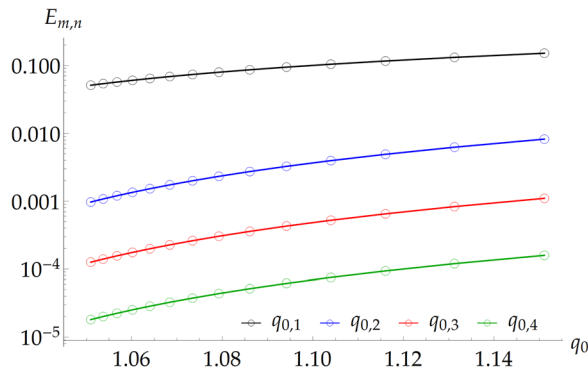


**FIG. 5.** Error defined according to Eq. (10) for  $q_{0,1}$  (black),  $q_{0,2}$  (blue),  $q_{0,3}$  (red), and  $q_{0,4}$  (green).

smaller than the cylindrical case considered by Waelbroeck and Hazeltine,<sup>19</sup> where  $\delta q \sim \mathcal{O}(\bar{\epsilon})$ . Setting  $\alpha_i = 0.045\bar{\epsilon}^{2i}/x_1^3$  and using Eq. (26), we can write

$$\frac{\delta W}{W_0} \approx \alpha_1 \int_0^1 x^3 (x - x_1) \zeta^2 dx - \alpha_2 \int_0^1 x^5 (x - x_1) \zeta^2 dx, \quad (33)$$

where the next non-vanishing order is  $\mathcal{O}(\bar{\epsilon}^2 \delta q^2)$ . Exploiting the breakdown of the standard parameter ordering that has been described in both the literature and present work is what affords the ability to estimate the critical value of the pressure gradient since the contributions that may be the next lowest in order, i.e.,  $\mathcal{O}(\bar{\epsilon}^2 \delta q^2)$ , may be stabilizing. We now use Eq. (33) to estimate the critical value of  $x_1$  (which describes localization of the pressure gradient) such that  $\delta W < 0$ . There are three conditions where the ordering in Eq. (33) is consistent. Namely, when  $\alpha_1 \approx \bar{\epsilon}$ ,  $\bar{\epsilon}^2$ , and  $\bar{\epsilon}^3$ . Respectively, we find

$$\alpha_1 \approx \bar{\epsilon} \rightarrow x_1 \approx 0.25, \Rightarrow \alpha_2 \approx 0.038 \sim \mathcal{O}(\bar{\epsilon}^3), \quad (34)$$

$$\alpha_1 \approx \bar{\epsilon}^2 \rightarrow x_1 \approx 0.35, \Rightarrow \alpha_2 \approx 0.012 \sim \mathcal{O}(\bar{\epsilon}^4), \quad (35)$$

$$\alpha_1 \approx \bar{\epsilon}^3 \rightarrow x_1 \approx 0.51, \Rightarrow \alpha_2 \approx 0.004 \sim \mathcal{O}(\bar{\epsilon}^5), \quad (36)$$

and note the small stabilizing contribution from  $\alpha_2$ . For the pressure profile and range of  $q_0$  under consideration, we expect a pressure-driven ( $m = 1, n = 1$ ) mode to be destabilized when  $0.25 \lesssim x_1 \lesssim 0.35$ . These qualitative predictions are subsequently validated in Sec. V.

For  $q_{0,i}$  with  $i > 1$ , the modes of interest are such that  $m/n \sim \mathcal{O}(1)$  and so  $\bar{\epsilon} \sim \mathcal{O}(\epsilon)$ , which remains approximately fixed. On the other hand,  $E_{m,n}(q_{0,i}) \approx M_n = 1/(\sqrt{5}n^2)$  implies  $\delta q \approx 1/(\sqrt{5}n^2)$  and, therefore, decreases as  $n$  becomes large. In the preceding discussion, we consider the modes associated with  $q_{0,2}$  and  $q_{0,3}$  for  $b \in [7, 20]$ . From Eq. (12), we find that this corresponds to  $7 \leq n \leq 20$  and  $20 \leq n \leq 59$ , respectively. For  $q_{0,2}$ , this implies  $0.001 \leq M_n \leq 0.009$  and  $\mathcal{O}(\bar{\epsilon}^6) \lesssim \delta q \lesssim \mathcal{O}(\bar{\epsilon}^4)$ , while for  $q_{0,3}$ , it follows  $0.0001 \leq M_n \leq 0.001$  and, therefore,  $\mathcal{O}(\bar{\epsilon}^8) \lesssim \delta q \lesssim \mathcal{O}(\bar{\epsilon}^6)$ .

For  $\delta q \lesssim \mathcal{O}(\bar{\epsilon}^3)$ , we find that the first non-zero term of Eq. (29) includes the  $i = 2$  term of the current-drive contribution, which is negative and, therefore, destabilizing. Note that the  $i = 1$  term, which is stabilizing, is of order  $\mathcal{O}(\bar{\epsilon}^2 \delta q^2)$  and, therefore, smaller than  $\mathcal{O}(\bar{\epsilon}^4 \delta q)$  when  $\delta q \lesssim \mathcal{O}(\bar{\epsilon}^3)$ . For the first two orders for  $q_{0,2}$  and  $q_{0,3}$ , we can, therefore, write

$$\begin{aligned} \frac{\delta W}{W_0} = & \bar{\epsilon}^4 \int_0^1 \delta q \left( \frac{B_z}{q} \right)^2 \left( 3q + \frac{m}{n} \right) x^3 \zeta^2 dx \\ & + \alpha_1 \int_0^1 x^3 (x - x_1) \zeta^2 dx - \bar{\epsilon}^2 \alpha_1 \int_0^1 x^5 (x - x_1) \zeta^2 dx, \end{aligned} \quad (37)$$

noting that the next non-vanishing terms are of order  $\mathcal{O}(\bar{\epsilon}^2 \delta q^2)$ . The first and second terms on the RHS of Eq. (37) correspond to stabilizing and destabilizing contributions from the parallel current and pressure gradient, respectively, while the third term is a stabilizing correction to the pressure drive. We can rewrite  $\alpha_i \approx 1.5 \times 10^{-5} (\bar{\epsilon}^{2i}) \Delta p / x_1^3$ , where  $\Delta p$  is the equilibrium parameter that describes the pressure difference across the zero-shear region (cf. Table I). For  $q_{0,2}$  ( $b = 7$ ), we see that when  $\alpha_1 > \mathcal{O}(\bar{\epsilon}^8)$ , the pressure gradient is the dominant contribution to Eq. (37) and destabilizing. This is achieved when  $\Delta p \approx 90x_1^3$ , and since  $x_1 < 1$ , even a small  $\Delta p$  is destabilizing, which is consistent with well-known results. For  $q_{0,2}$  ( $b = 20$ ), the corresponding results require  $\Delta p \approx 10x_1^3$ . Thus, for all  $x_1$  and  $q_0$  considered, the pressure-driven modes associated with  $q_{0,2}$  and  $q_{0,3}$  are unstable. Finally, we note that as  $\delta q$  decreases, the current term becomes unimportant since  $\alpha_1$  is independent of  $\delta q$ , and Eq. (37) reduces to Eq. (33).

## V. NUMERICAL PARAMETER SCANS AND VALIDATION OF PREDICTIONS

To test the predictions made in Secs. III and IV, we use the initial-value extended-MHD code, M3D-C<sup>1</sup>,<sup>13</sup> to solve for the non-ideal, linear plasma evolution for  $x_1 \in [0.1, 0.4]$  and  $q_0$  corresponding to  $b \in [7, 20]$ . Specifically, we solve the single fluid dissipative MHD equations with isotropic transport parameters in cylindrical geometry given by<sup>13</sup>

$$\frac{\partial \tilde{n}}{\partial t} + \nabla \cdot (\tilde{n} \mathbf{u}) = 0, \quad (38)$$

$$\tilde{n} m_i \left( \frac{\partial \mathbf{u}}{\partial t} + \mathbf{u} \cdot \nabla \mathbf{u} \right) = \mathbf{J} \times \mathbf{B} - \nabla p - \nabla \cdot \Pi + \mathbf{F}, \quad (39)$$

$$\frac{\partial p}{\partial t} + \mathbf{u} \cdot \nabla p + \Gamma p \nabla \cdot \mathbf{u} = (\Gamma - 1) [Q - \nabla \cdot \mathbf{q} + \eta J^2 - \mathbf{u} \cdot \mathbf{F} - \Pi : \nabla \mathbf{u}], \quad (40)$$

$$\mathbf{E} = -\mathbf{u} \times \mathbf{B} + \eta \mathbf{J}, \quad (41)$$

$$\mathbf{J} = \frac{1}{\mu_0} \nabla \times \mathbf{B}, \quad (42)$$

$$\frac{\partial \mathbf{B}}{\partial t} = -\nabla \times \mathbf{E}, \quad (43)$$

where  $\tilde{n}$  is the number density,  $\mathbf{u}$  is the fluid velocity,  $\mathbf{E}$  is the electric field,  $m_i$  is the ion mass,  $\Pi$  is the viscous stress tensor,  $\Gamma$  is the ratio of specific heats, and  $\mathbf{F}$  and  $Q$  denote external forces and heat sources, respectively. For the thermal conductivity,  $\mathbf{q}$ , we choose

$$\mathbf{q} = -\kappa_t \nabla T, \quad (44)$$

where  $T = T_e + T_i$ , and  $T_e$  and  $T_i$  are the electron and ion temperatures, respectively. In addition to the parameters given in Table I, we choose isotropic values of resistivity and viscosity such that  $P_m \equiv \nu/\eta = 10^{-2}$  and  $\kappa_t = 1 \text{ W/mK}$ . For  $0.2 < x_1 \leq 0.4$ , we use a uniform unstructured mesh with 21k elements. To ensure adequate resolution of mode structures when  $x_1 \leq 0.2$ , we use mesh packing in the region  $x \leq 0.25$ .

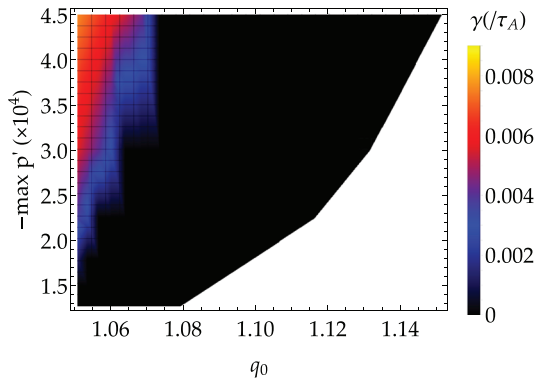


**FIG. 6.** Growth rates,  $\gamma$ , of the  $(m = 1, n = 1)$  nonresonant, pressure-driven mode corresponding to  $q_{0,1}$  for  $b \in [7, 20]$  and  $x_1 \in [0.1, 0.35]$ . Here,  $\max p'$  is given by Eq. (28) and corresponds to the value of the maximum pressure gradient. In the unshaded region, the mode is stable.

In Fig. 6, we plot linear growth rates,  $\gamma$ , of the  $(m = 1, n = 1)$  nonresonant, pressure-driven modes associated with  $q_{0,1}$  for  $b \in [7, 20]$  and  $x_1 \in [0.1, 0.35]$ , as a function of the maximum pressure gradient,  $\max p'$ , given by Eq. (28), where  $\max p' \propto 1/x_1$ . Stability is denoted by the unshaded region and, as expected, coincides with larger  $q_0$  and lower values of  $\max p'$ , corresponding to comparatively weak localization of the central pressure gradient. In a large subset of the parameter space considered, the  $(m = 1, n = 1)$  mode is marginally stable and its linear evolution is characterized by stable oscillations, due to  $\text{Re}(\gamma) = 0$  and  $\text{Im}(\gamma) \neq 0$ . For  $\max p' \lesssim -2 \times 10^4$  and  $q_0 \lesssim 1.068$ , the  $(m = 1, n = 1)$  mode is destabilized, and we find that  $\gamma$  grows with decreasing  $q_0$  and increasing  $\max p'$ , corresponding to greater localization of  $\nabla p$ , as expected.

In Fig. 7, we plot  $\gamma$  of the  $(m = 1, n = 1)$  mode as a function of  $q_0$  for  $x_1 = 0.1$  (which corresponds to  $\max p' = -4.5 \times 10^4$ ) and observe that the mode is unstable for  $q_0 \lesssim 1.07$ . Meanwhile, Fig. 8 shows  $\gamma$  of the  $(m = 1, n = 1)$  mode as a function of  $\max p'$  for  $q_0 = 1.051$ . In the unstable regime,  $\gamma$  appears to scale approximately linearly in  $q_0$ . From Fig. 6, the behavior appears to be consistent for other values of  $q_0$ , for which the  $(m = 1, n = 1)$  mode is unstable. For the most pessimistic case, the  $(m = 1, n = 1)$  mode is destabilized

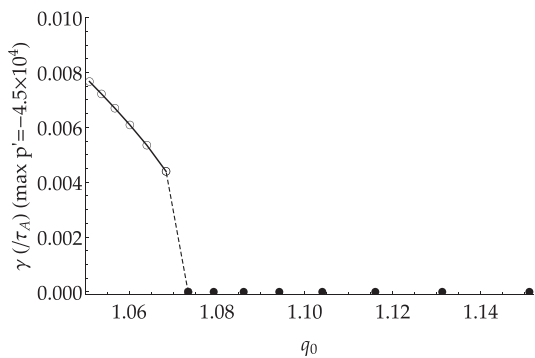


**FIG. 7.** Growth rates,  $\gamma$ , of the  $(m = 1, n = 1)$  nonresonant, pressure-driven mode corresponding to  $q_{0,1}$  for  $x_1 = 0.1$ , which corresponds to  $\max p' = -4.5 \times 10^4$ . Stability is denoted by filled circles.

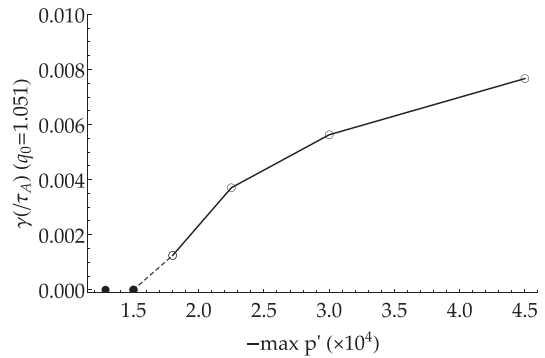


**FIG. 8.** Growth rates,  $\gamma$ , of the  $(m = 1, n = 1)$  nonresonant, pressure-driven mode corresponding to  $q_{0,1}$  for  $q_0 = 1.051$ . Stability is denoted by filled circles.

for  $\max p' \approx -1.8 \times 10^4$  which corresponds to  $x_1 = 0.25$ , in good agreement with Eqs. (34) and (35). As a function of  $q_0$ , destabilization of the mode occurs when  $q_0 \approx 1.068$ , which is consistent with the results of Kirby.<sup>8</sup>

In Fig. 9, we plot growth rates,  $\gamma$ , of nonresonant, pressure-driven  $(m = b + 1, n = b)$  modes for  $b \in [7, 20]$  and  $x_1 \in [0.1, 0.4]$ , which correspond to  $q_{0,2}$ . As predicted from Eq. (37), the modes are all unstable in the parameter regime considered. Comparing Figs. 6 and 9, we find that the growth rates of the  $(m = 1, n = 1)$  modes are maximized where  $\gamma$  values of the  $(m = b + 1, n = b)$  modes are minimized, namely, when  $\max p'$  is large and  $q_0$  is smallest. In particular, for the parameter range considered  $\max(\gamma)$  corresponds to an  $(m = 21, n = 20)$  mode. Even so, the growth rates of the  $(m = b + 1, n = b)$  modes, which correspond to  $q_{0,2}$ , are larger by at least a factor of two and, thus, dominate the linear evolution on an ideal timescale.

In Eq. (37), we identified a destabilizing contribution from the pressure gradient a stabilizing pressure gradient term due to a higher-order correction. Evidently, as the negative pressure gradient term is destabilizing and the dominant contribution to  $\delta W$  for the parameter ordering considered, the modes are unstable. Both the remaining

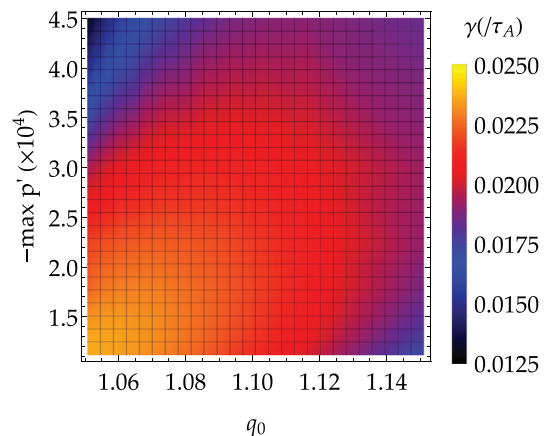


**FIG. 9.** Growth rates,  $\gamma$ , of the nonresonant, pressure-driven  $(m = b + 1, n = b)$  modes for  $b \in [7, 20]$  and  $x_1 \in [0.1, 0.4]$ , which correspond to  $q_{0,2}$ . The modes are unstable for all values of  $b$  and  $q_0$  considered.

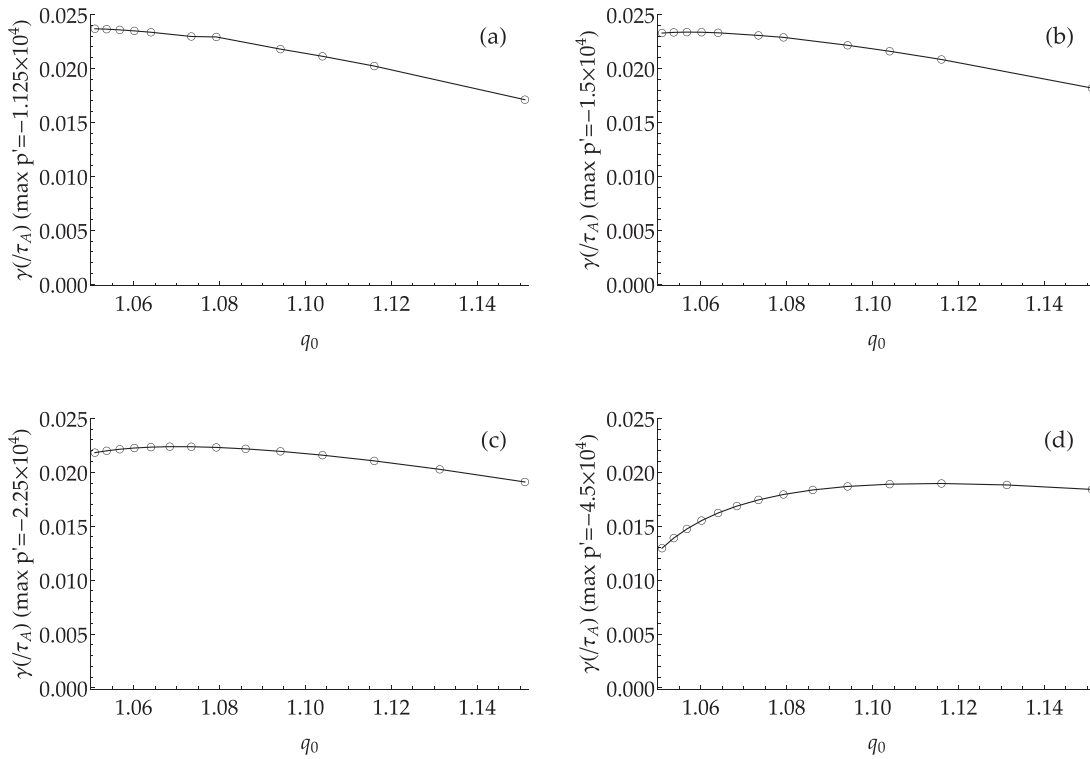


**FIG. 10.** Growth rates,  $\gamma$ , of nonresonant, pressure-driven ( $m = b + 1, n = b$ ) modes corresponding to  $q_{0,2}$  for (a)  $-1.125 \times 10^4$ , (b)  $-1.5 \times 10^4$ , (c)  $-2.25 \times 10^4$ , and (d)  $-4.5 \times 10^4$  with  $b \in [7, 20]$ .

terms are subdominant but can, nonetheless, either enhance or reduce  $\gamma$  by modifying  $\delta W$ , since the linear growth rate can be estimated approximately as the ratio of the potential to kinetic energies.<sup>23</sup> Recall that the current term is included in Eq. (37) when  $\delta q \ll \mathcal{O}(\bar{\epsilon}^3)$ . Thus, while it is unimportant for the ( $m = 1, n = 1$ ) modes considered in Figs. 6–8, the growth rates of the modes considered in Fig. 9 are modified by a contribution from the current. Whereas the current drive is linear in  $\delta q$  and vanishes as  $n \rightarrow \infty$ , the stabilizing pressure gradient contribution is independent of  $\delta q$ . The two subdominant terms are, thus, most comparable when  $\max p'$  is small and  $q_0$  is not too large. As the two parameters increase and decrease, respectively, the change to  $\gamma$  due to current becomes small while the pressure gradient remains an  $\mathcal{O}(\bar{\epsilon}^2)$  correction to the dominant, destabilizing pressure drive.

To further illustrate this effect, in Fig. 10, we compare  $\gamma$  of the ( $m = b + 1, n = b$ ) modes as a function of  $q_0$  for four representative values of  $\max p'$ , namely, (a)  $-1.125 \times 10^4$ , (b)  $-1.5 \times 10^4$ , (c)  $-2.25 \times 10^4$ , and (d)  $-4.5 \times 10^4$ . For the modes considered,  $\gamma$  is clearly maximized for  $q_{0,2}$  ( $b = 20$ ) when  $\max p'$  is smallest, and, as expected, the growth rate is minimized in Fig. 10(d) where  $\max p'$  is maximized and  $\delta q$  is smallest. Simultaneously, as  $\delta q$  increases,  $\delta q$  approaches  $\mathcal{O}(\bar{\epsilon}^3)$  at which point the ordering applied in Eq. (37) breaks down. For large values of  $\delta q$ , the subdominant correction terms are of order  $\mathcal{O}(\bar{\epsilon}^2 \delta q^2)$  and stabilizing, which likely explains the overall decrease in  $\gamma$  observed in Fig. 10 as  $q_0$  increases.

As an illustrative example, in Fig. 11, we compare the growth rates of the ( $m = 8, n = 7$ ) and ( $m = 23, n = 20$ ) modes which correspond to  $q_{0,2}$  and  $q_{0,3}$  for  $q_0$  ( $b = 7$ )  $\approx 1.151$ , respectively, as a function of  $\max p'$ . For the ( $m = 3b + 2, n = 3b - 1$ ) mode that corresponds to  $q_{0,3}$ ,  $\gamma$  behaves consistently with the preceding observations, namely,  $\gamma$  is maximized for small  $\max p'$  and decreases with increasing  $\max p'$ . The stronger decrease with increasing  $\max p'$ , when compared to the ( $m = 8, n = 7$ ) mode, can be understood by the fact that  $\delta q$  scales approximately with  $n^{-2}$  for both  $q_{0,2}$  and  $q_{0,3}$ . The

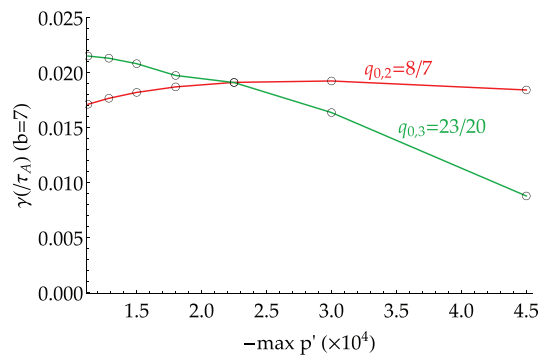


**FIG. 11.** Growth rates,  $\gamma$ , of the nonresonant, pressure-driven ( $m = 8, n = 7$ ) (red) and ( $m = 23, n = 20$ ) (green) modes, which correspond to  $q_{0,2}$  and  $q_{0,3}$ , respectively, for  $q_0$  ( $b = 7$ )  $\approx 1.151$ , with  $x_1 \in [0.1, 0.4]$ .

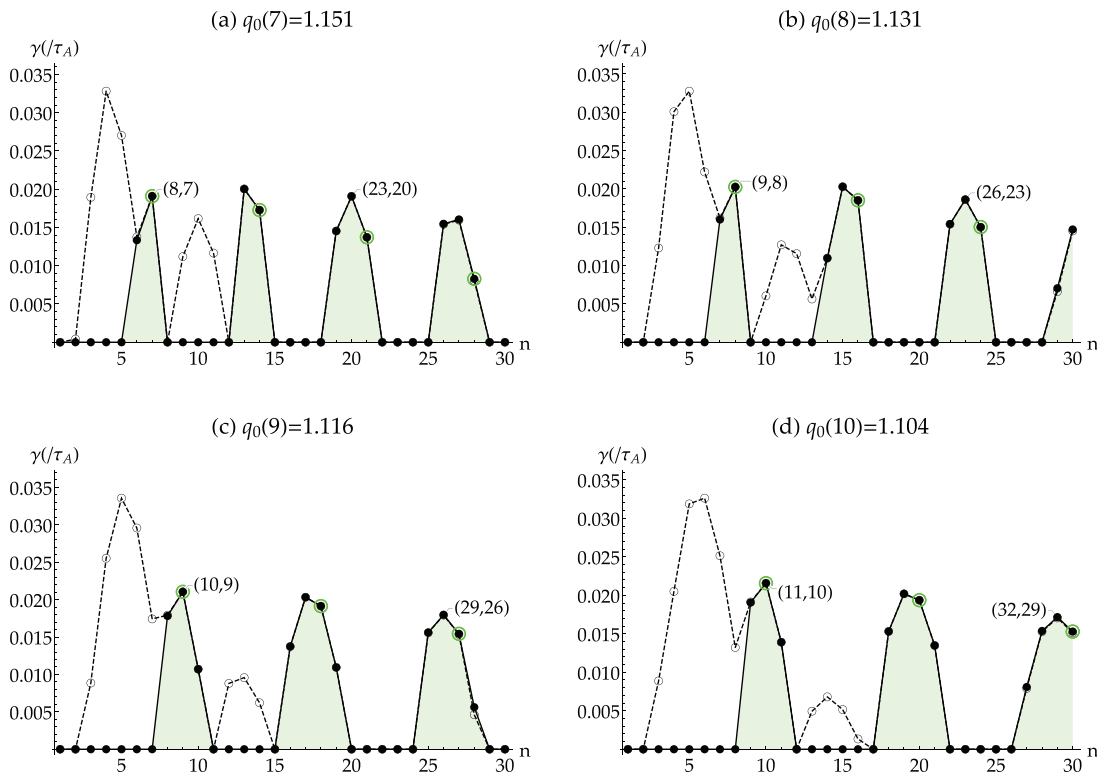


**FIG. 12.** Growth rates,  $\gamma$ , of the fastest growing linear instability with  $n \in [1, 30]$  and  $\max p' = -2.25 \times 10^4$  for (a)  $q_0(b=7) = 1.151$ , (b)  $q_0(b=8) = 1.131$ , (c)  $q_0(b=9) = 1.116$ , and (d)  $q_0(b=10) = 1.104$ . Growth rates computed using the full equilibrium (hollow circles, dashed lines) are plotted with growth rates computed with the ideal wall placed at  $x_1 = 0.2$  (filled circles, solid line), where  $q = q_0$  everywhere and there are no resonances in the plasma volume. The  $(m = b + 1, n = b)$  and  $(m = 3b + 2, n = 3b - 1)$  modes corresponding to  $q_{0,2}$  and  $q_{0,3}$ , respectively, are labeled. Green circles denote harmonics of the  $(m = b + 1, n = b)$  modes. In (a)–(d), the peak growth rates in the second (from left) band of unstable modes correspond to the (15, 13), (17, 15), (19, 17), and (21, 19) modes, respectively, which are associated with convergents of  $q_0$  that do not satisfy Eq. (10).

growth rate modification due to the current term in Eq. (37) decreases with  $\delta q$  and, thus, approaches zero faster for  $q_{0,3}$  than  $q_{0,2}$ . We remark that the competing effects of the subdominant pressure gradient and current contributions evident in Figs. 9–11 suggest an identifiable parameter range where such modes are most unstable and, thus, may be avoided.

Thus far, we have focused on the behavior of the modes associated with convergents ( $q_{0,i}$ ) of different  $q_0$  and, therefore, different toroidal mode numbers. To demonstrate that these modes are, indeed, “special,” in Fig. 12, we plot growth rates of the fastest growing linear instability for each  $n \in [1, 30]$  for  $q_0(b=7) = 1.151$ ,  $q_0(b=8) = 1.131$ ,  $q_0(b=9) = 1.116$  and  $q_0(b=10) = 1.104$ , where  $\max p' = -2.25 \times 10^4$ .

In addition to the pressure-driven nonresonant modes associated with Eq. (12), the discontinuities in  $J_{\parallel}$  at the internal boundaries of the equilibria ( $x_1$  and  $x_2$ ) may be an additional source of instabilities. As noted by Wright *et al.*,<sup>15</sup> these arise due to limited smoothness of the equilibrium profiles and are distinct from the pressure-driven modes of primary interest.

Characteristic radial mode structures of the current-discontinuity-driven and nonresonant pressure-driven instabilities are given in Fig. 13. It can be seen that the former is highly localized about the discontinuity in  $J_{\parallel}$ , which occurs at the internal boundary  $x_1$  and

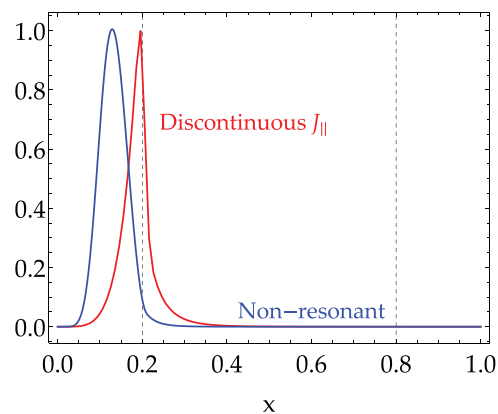


**FIG. 13.** Characteristic radial mode structures of the current-density-discontinuity-driven (red) and nonresonant pressure-driven (blue) instabilities considered. The internal boundaries are located at  $x = x_1$  and  $x_2$  and denoted by vertical dashed lines. For nonresonant modes, the displacement extends over a large fraction of the zero-shear region. By contrast, the current-density-discontinuity driven instability is strongly peaked about the discontinuity in  $J_{\parallel}$  at  $x = x_1$  (denoted by the leftmost vertical dashed line).

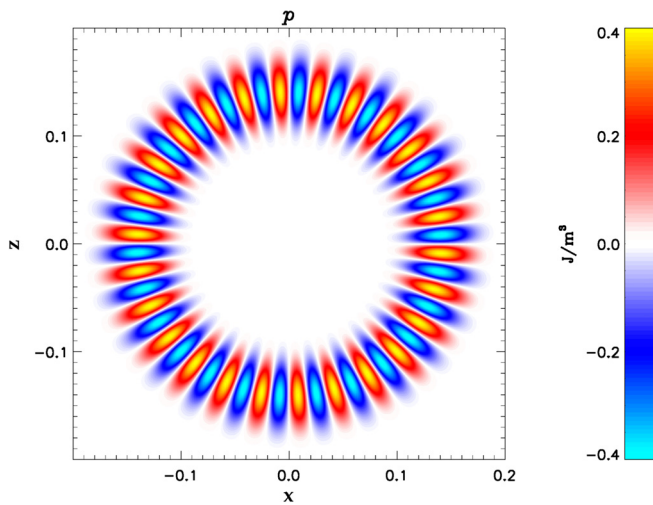


**FIG. 14.** The perturbed pressure profile for a nonresonant pressure-driven ( $m = 26$ ,  $n = 23$ ) mode, which corresponds to  $q_{0,3}(b = 8)$ . The profile exhibits a radially extended structure and is consistent with the expected perturbation due to an interchange mode.

corresponds to the edge of the shear-free core region. By contrast, the nonresonant pressure-driven mode exhibits a globally extended mode structure in the low shear region. A characteristic profile of the perturbed pressure for the nonresonant modes of interest is shown in Fig. 14. In addition to the radially extended structure, as was evident in Fig. 13, the profile exhibits structure that is characteristic of an interchange mode.

To isolate the modes associated purely with nonresonant effects, we performed an additional scan for  $n \in [1, 30]$  with the ideal wall placed at  $x = x_1 = 0.2$  so that  $q = q_0$  throughout the plasma volume, meaning that there are no resonant surfaces in the plasma. The growth rates from both scans are overlaid in Fig. 12.

That the growth rates associated with the nonresonant instabilities in both scans overlap almost identically in Fig. 12 confirm that the effects described in the preceding analysis are the dominant cause of these instabilities. For each  $q_0$  considered, we observe that the  $(m = b + 1, n = b)$  and  $(m = 3b + 2, n = 3b - 1)$  modes corresponding to  $q_{0,2}$  and  $q_{0,3}$  are the dominant instability. We find that harmonics of  $(m = b + 1, n = b)$  (associated with  $q_{0,2}$ ) are also unstable, with  $\gamma$  decreasing with increasing  $n$  as expected. In the purely nonresonant case, the remaining unstable modes correspond to side bands, i.e.,  $m + 1$  and/or  $m - 1$  (and harmonics thereof), of the earlier identified nonresonant modes. We note that the fundamental harmonics of the additional unstable modes have poloidal and toroidal mode numbers such that  $m/n$  are convergents of  $q_0$  but which do not satisfy Eq. (10). This suggests that bound on  $E_{m,n}$  given by Hurwitz's theorem may be overly stringent and motivates further work, presently under way, to identify additional criteria for predicting unstable nonresonant modes.

## VI. DISCUSSION AND CONCLUSIONS

Nonresonant MHD instabilities, i.e., modes with a poloidal and toroidal mode number such that  $q \neq m/n$ , are associated with spatially extended linear displacements. Equilibria that are unstable to

multiple nonresonant modes may be particularly susceptible to global loss of confinement resulting from nonlinear interactions and magnetic field line chaos. It is, therefore, important to be able to predict which nonresonant modes are likely to be unstable. In this work, we studied nonresonant pressure-driven MHD modes in the large-aspect-ratio tokamak limit. We considered equilibria with zero shear in the plasma core,  $q_0$  irrational and a central pressure gradient, consistent with pre-crash profiles in sawtooth tokamak plasmas.

Representing  $q_0$  as a continued fraction and constructing convergents, we developed a predictive criterion for identifying the unstable nonresonant modes. The convergents are rational approximations of  $q_0$  obtained by truncating the continued fraction at a finite depth and correspond to nonresonant modes likely to be unstable. We considered specifically convergents satisfying Hurwitz's theorem, which gives a stringent upper bound on the error of the rational approximation for  $q_0$ .

By performing a higher-order analysis of the standard Energy Principle, which explicitly treated the nonresonant parameter  $\delta q$ , we were able to unify understanding of nonresonant pressure-driven modes, particularly the  $(m = 1, n = 1)$  quasi-interchange mode and infernal modes, which tend to be higher  $m$  and  $n$ . This allowed us to determine the conditions under which nonresonant modes can be expected to dominate and predict the critical central pressure gradient for destabilization of the  $(m = 1, n = 1)$  mode.

For a range of  $q_0 > 1$ , we computed linear growth rate spectra as a function of toroidal mode number,  $\gamma(n)$ , using the initial-value extended-MHD code, M3D-C<sup>13</sup>. We find a preponderance of fast-growing non-ideal, nonresonant modes with moderate to high  $n$ . Importantly, the  $\gamma(n)$  spectra shown in Fig. 12 recover the characteristic structure first observed by Manickam *et al.*<sup>3</sup> for ideal infernal modes, and radially extended mode structures are observed in both cases. This strongly suggests that the qualitative  $\gamma(n)$  spectrum of infernal modes is associated with nonresonance in low shear equilibria. When  $q_0$  is irrational and the shear sufficiently low in the plasma core, we predict that the unstable modes correspond to convergents of  $q_0$ .

In the work of Manickam *et al.*,<sup>3</sup> the peaks of the  $\gamma(n)$  spectrum did not coincide with integer  $n$ , which was treated as a continuous parameter. On qualitatively accounting for the fact that actual modes have integer mode numbers, the peaks in  $\gamma(n)$  observed by Manickam *et al.*<sup>3</sup> are consistent with our results. Although infernal modes have been considered from the perspective of ballooning theory,<sup>3,20,25–27</sup> the absence of ballooning physics in the present work suggests an underlying effect associated with nonresonance and properties of the equilibrium  $q$ -profile in the low shear region. We contend that these effects persist in toroidal geometry and, therefore, can be used to predict the unstable nonresonant modes, in analogy with the criterion developed in this work. Specifically, the nonresonant modes most likely to be unstable can be associated with the convergents of the continued fraction representation of  $q_0$  for monotonically increasing  $q$ -profiles and—potentially— $q_{min}$  for sufficiently weak reversed shear profiles.

We now briefly sketch how cylindrical picture is expected to be modified by toroidicity for a low shear equilibrium where  $q_0$  is irrational. As before, we construct convergents,  $q_{0,i}$ , of  $q_0$ , which form a sequence with monotonic increasing denominators that correspond to the toroidal mode number of the associated nonresonant modes. We assume the plasma is stable to high- $n$  ballooning modes, which is valid in the infernal mode regime.<sup>3</sup> Since the denominators of the

convergent modes correspond to the toroidal mode number and rapidly become large, we anticipate that the first few convergents are the most important. These correspond to modes with moderate to high poloidal and toroidal mode numbers. This is consistent with the  $\gamma(n)$  spectra obtained by Manickam *et al.*,<sup>3</sup> which decayed rapidly for larger  $n$ .

The ability to identify unstable nonresonant pressure-driven modes, which have been invoked in some models for sawtooth crashes,<sup>6,8</sup> enables prediction of the radial extent of temperature and pressure flattening in post-sawtooth-crash profiles for these models. As the central  $q$ -profile is flattened, for example, due to generation of a dynamo<sup>28</sup> while sufficient heating is applied to maintain central peaking of the pressure profile,<sup>6</sup> nonresonant, high- $n$  pressure-driven modes, which would otherwise be suppressed by shear, approach marginal stability. The crash itself may be precipitated by destabilization of  $n > 1$  harmonics of the  $(n, n)$  interchange mode.<sup>6,8</sup> As nonlinear interactions reduce the localization of the central pressure gradient, nonresonant modes, identified in this work to be more unstable as  $\max p'$  decreases, may be destabilized, leading to a cascade that may ultimately determine the width of the chaotic field, i.e., the temperature- and pressure-flattened region, following a crash.

## ACKNOWLEDGMENTS

This work was supported by an Australian Government Research Training Program (RTP) Scholarship, DOE Contract No. DEAC02-76CH03073, Australian Research Council grant DP170102606, and a grant from the Simons Foundation/SFARI (560651, AB).

## DATA AVAILABILITY

The data that support the findings of this study are available from the corresponding author upon reasonable request.

## REFERENCES

- I. B. Bernstein, E. A. Frieman, M. D. Kruskal, and R. M. Kulsrud, "An energy principle for hydromagnetic stability problems," *Proc. R. Soc. London. Ser. A. Math. Phys. Sci.* **244**(1236), 17–40 (1958).
- C. Gormezano, A. C. C. Sips, T. C. Luce, S. Ide, A. Becoulet, X. Litaudon, A. Isayama, J. Hobirk, M. R. Wade, T. Oikawa, R. Prater, A. Zvonkov, B. Lloyd, T. Suzuki, E. Barbato, P. Bonoli, C. K. Phillips, V. Vdovin, E. Joffrin, T. Casper, J. Ferron, D. Mazon, D. Moreau, R. Bundy, C. Kessel, A. Fukuyama, N. Hayashi, F. Imbeaux, M. Murakami, A. R. Polevoi, and H. E. S. John, "Chapter 6: Steady state operation," *Nucl. Fusion* **47**(6), S285–S336 (2007).
- J. Manickam, N. Pomphrey, and A. M. M. Todd, "Ideal MHD stability properties of pressure driven modes in low shear tokamaks," *Nucl. Fusion* **27**(9), 1461–1472 (1987).
- L. A. Charlton, B. A. Carreras, and V. E. Lynch, "Linear and nonlinear properties of infernal modes," *Phys. Fluids B* **2**(7), 1574–1583 (1990).
- H. A. Holties, G. T. A. Huysmans, J. P. Goedbloed, W. Kerner, V. V. Parail, and F. X. Soldner, "Stability of infernal and ballooning modes in advanced tokamak scenarios," *Nucl. Fusion* **36**(8), 973 (1996).
- S. C. Jardin, I. Krebs, and N. Ferraro, "A new explanation of the sawtooth phenomena in tokamaks," *Phys. Plasmas* **27**(3), 032509 (2020).
- J. A. Wesson, "Sawtooth oscillations," *Plasma Phys Controlled Fusion* **28**(1A), 243 (1986).
- K. Kirby, "Numerical simulations of ideal internal kink modes with flat central  $q$ -profile," *Nucl. Fusion* **28**(2), 231 (1988).
- B. V. Chirikov, "A universal instability of many-dimensional oscillator systems," *Phys. Rep.* **52**(5), 263–379 (1979).
- R. L. Dewar, T. Tatsuno, Z. Yoshida, C. Nührenberg, and B. F. McMillan, "Statistical characterization of the interchange-instability spectrum of a separable ideal-magnetohydrodynamic model system," *Phys. Rev. E* **70**(6), 066409 (2004).
- T. Tatsuno, M. Wakatani, and K. Ichiguchi, "Ideal interchange instabilities in stellarators with a magnetic hill," *Nucl. Fusion* **39**(10), 1391 (1999).
- R. J. Hastie, "Sawtooth instability in tokamak plasmas," *Astrophys. Space Sci.* **256**(1–2), 177–204 (1997).
- S. C. Jardin, N. Ferraro, J. Breslau, and J. Chen, "Multiple timescale calculations of sawteeth and other global macroscopic dynamics of tokamak plasmas," *Comput. Sci. Disc.* **5**(1), 014002 (2012).
- S. R. Hudson and B. F. Kraus, "Three-dimensional magnetohydrodynamic equilibria with continuous magnetic fields," *J. Plasma Phys.* **83**(4), 715830403 (2017).
- A. M. Wright, S. R. Hudson, R. L. Dewar, and M. J. Hole, "Resistive stability of cylindrical MHD equilibria with radially localized pressure gradients," *Phys. Plasmas* **26**(6), 062117 (2019).
- D. Brunetti, J. P. Graves, E. Lazzaro, A. Mariani, S. Nowak, W. A. Cooper, and C. Wahlberg, "Analytic study on low- $n$  external ideal infernal modes in tokamaks with large edge pressure gradients," *J. Plasma Phys.* **84**(2), 745840201 (2018).
- W. Rudin, *Principles of Mathematical Analysis* (McGraw-Hill New York, 1964).
- I. M. Niven, *Diophantine Approximations* (Courier Corporation, 2008).
- F. L. Waelbroeck and R. D. Hazeltine, "Stability of low-shear tokamaks," *Phys. Fluids* **31**(5), 1217–1223 (1988).
- L. A. Charlton, R. J. Hastie, and T. C. Hender, "Resistive 'infernal' modes," *Phys. Fluids B* **1**(4), 798–803 (1989).
- R. J. Hastie and T. C. Hender, "Toroidal internal kink stability in tokamaks with ultra flat  $q$  profiles," *Nucl. Fusion* **28**(4), 585 (1988).
- J. P. Freidberg, *Ideal MHD* (Cambridge University Press, 2014).
- V. D. Shafranov, "Hydromagnetic stability of a current-carrying pinch in a strong longitudinal magnetic field," *Sov. Phys. Tech. Phys.* **15**, 175 (1970).
- B. R. Suydam, "Stability of a linear pinch," *J. Nucl. Energy* (1954) **7**(3–4), 275–276 (1958).
- L. E. Zakharov, "The theory of hydromagnetic stability of a tokamak plasma," *Nucl. Fusion* **18**(3), 335 (1978).
- R. L. Dewar, "Ballooning mode schrödinger equation," In *Theory of Fusion Plasmas Società Italiana di Fisica, Editrice Compositori. Proceedings of the Varenna Workshop on Theory of Fusion Plasmas, Varenna, Italy, August 24–28 1987*, edited by E. Sindoni, A. Bondeson, and F. Troyon (Bologna, 1988), pp. 107–121.
- R. L. Dewar, "Spectrum of the ballooning Schrödinger equation," *Plasma Phys. Controlled Fusion* **39**(3), 453 (1997).
- S. C. Jardin, N. Ferraro, and I. Krebs, "Self-organized stationary states of tokamaks," *Phys. Rev. Lett.* **115**(21), 215001 (2015).